Article

Ag₂S Nanoparticles Supported on 3D Flower-Shaped Bi₂WO₆ Enhanced Visible Light Catalytic Degradation of Tetracycline

Hengcan Dai,* Xiaoliang Yang, and Fei Tang
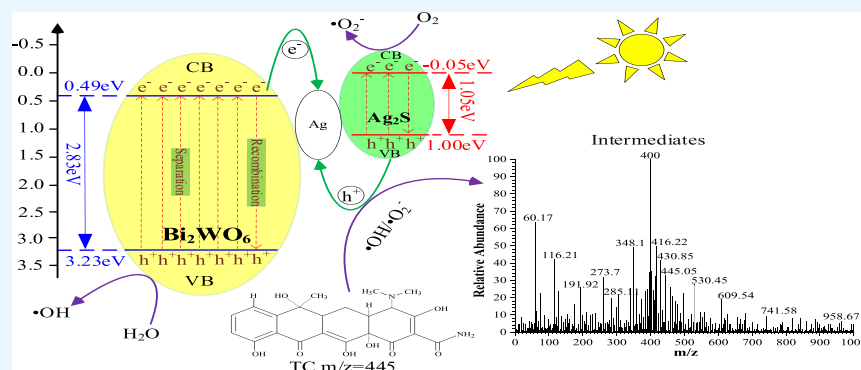
Read Online

ACCESS | Metrics & More | Article Recommendations

ABSTRACT: A three-dimensional flower-shaped Bi₂WO₆ has been prepared by a hydrothermal procedure without the addition of an auxiliary agent and under neutral conditions with ultrapure water serving as solvent, and the Ag₂S−Bi₂WO₆ composite with weight ratios of 5, 10, and 15% was prepared by a hydrothermal method. The crystallinity, morphology, mode of binding, and optical properties of the Ag₂S−Bi₂WO₆ composite were characterized, the results of which showed that the composite had excellent dispersion, crystallinity, and purity. The composite with a weight ratio of 10% had the best photocatalytic performance, and the degradation rate of tetracycline reached 95.51% within 120 min, an increase of 27.35% over Bi₂WO₆. In experiments, some focus was given to the effect of the initial solution pH and the concentrations of humic acid and inorganic anions on the degradation efficiency. Based on free radical capture experiments and the semiconductor theory, the main active substances and mechanisms in the optical catalytic reaction process were studied, and speculation was given concerning the degradation pathway for the target pollutants. This study has conceived novel methods for the development of dual semiconductor systems consisting of a Ag NP composite and in doing so has provided new approaches for the development and photocatalysis for water pollution control.

1. INTRODUCTION

Because of persistence, accumulation, and ecological toxicity, antibiotics not only affect the ecological balance in the environment but also pose a serious threat to human health.[1−4] Numerous studies have focused on the degradation method of antibiotics, such as adsorption,[5] microbial degradation,[6] Fenton,[7] photocatalysis,[8] and electrochemistry.[9] Photocatalysis, as an advanced oxidation technology for energy saving and environmental protection, is widely used not only in hydrogen evolution and carbon dioxide reduction[10] but also in water treatment because it can degrade pollutants into easily biodegradable intermediates in a short time or can directly mineralize H_2O and CO_2.[11,12]

Bi₂WO₆ is the simplest Aurivillius-type oxide, which is alternately composed of a $[WO_4]^{2-}$ octahedral perovskite layer and a $[Bi_2O_2]^{2+}$ ion layer. Its unique crystal structure enables it to have catalytic, piezoelectric, and oxygen ionization physical and chemical properties. Because of its small band gap and open layered void structure, which can provide more active

sites for photocatalytic reaction, it has become one of the concerned photocatalytic materials. However, Bi₂WO₆ still has limitations such as the photogenic electron−hole high compound rate and slow charge transfer rate, which seriously limit its use in industry.[13−15] As recorded in the literature, through semiconductor recombination, there is a matching band structure between semiconductors, and the spectral response range of Bi₂WO₆ can be broadened by using the band overlap effect; the transfer of the photogenerated electron−hole pairs was promoted, such as AgBr/Bi₂WO₆,[16] Bi₂WO₆/ZnWO₄,[17] Al₂(WO₄)₃/Bi₂WO₆,[18] and AgI/Bi₂WO₆.[19] Metal
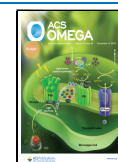
sulfides are important narrow-band-gap semiconductor materials that typically have excellent visible light absorption ability.[20] As one of them, silver sulfide (Ag_2S) is a good candidate for Bi_2WO_6 photosensitization due to its fast charge exchange properties, narrow band gap, and high stability as a nontoxic semiconductor.[21,22]

In this study, it is proposed for the first time that Ag_2S and three-dimensional flower-shaped Bi_2WO_6 can form a novel dual semiconductor system by changing the preparation conditions of the precipitation method, and it has a different morphology, visible light responsiveness, and degradation mechanism compared with previous studies. The photocatalytic performance of the composite was studied by photocatalytic degradation of tetracycline (TCH), and the effects of the initial solution pH, the humic acid (HA) concentration, and different inorganic anions on the degradation efficiency are discussed to clarify the stability of the catalyst to water condition change.

2. METHOD

2.1. Preparation of Bi_2WO_6. All chemicals were of analytical purity and used without further purification. First, 9.70 g (20 mmol) $Bi(NO_3)_3 \cdot 5H_2O$ and 3.30 g (10 mmol) $Na_2WO_4 \cdot 2H_2O$ were, respectively, dispersed in 40 mL of ultrapure water and stirred for 40 min. Then, $Na_2WO_4 \cdot 2H_2O$ solution was added to $Bi(NO_3)_3 \cdot 5H_2O$ solution slowly, and magnetic stirring was performed for 50 min. The resulting solution was reacted hydrothermally at 200 °C for 12 h. Subsequently, the precipitate was rinsed three times alternately with ultrapure water and ethanol, filtered, and then dried at 70 °C for 10 h, yielding the Bi_2WO_6 sample.

2.2. Preparation of $Ag_2S-Bi_2WO_6$. Bi_2WO_6 (1.00 g) was dispersed in 40 mL of ultrapure water and stirred for 30 min; then, 0.005 g of sodium dodecyl benzenesulfonate (SDBS) was added to the solution and stirred for 5 h. A small amount of $AgNO_3$ was dissolved in 30 mL of ultrapure water and then added to the Bi_2WO_6 solution and stirred for 2 h. A corresponding weight of $Na_2S \cdot 9H_2O$ was dissolved in 20 mL of ultrapure water, which was then added to the above solution, and the mixture was stirred continuously for 2 h. The samples were washed three times with ethanol and ultrapure water, respectively; filtered; and then dried at 70 °C for 12 h. $Ag_2S-Bi_2WO_6$ composites with weight ratios of 5% (wt 5% BWO), 10% (wt 10% BWO), and 15% (wt 15% BWO) were prepared.

2.3. Characterization and Instrumental Parameters. The crystallinity of the samples was characterized by a D/max-2200X X-ray diffractometer (XRD) with a Cu target, the tube voltage was set at 40 kV, and the diffraction angle ranged from 10 to 80°. A Quanta 200 cold field emission scanning electron microscope (SEM) was used to characterize the structural morphology of the samples, with the SEM being equipped with a GENESIS4000 energy dispersive X-ray spectrometer; the working voltage was 3−5 kV. The chemical bonding of the samples was studied using an ESCALAB 250 X-ray photoelectron spectroscopy analyzer (XPS). The binding energy in the spectrum was calibrated by C 1s (284.62 eV); the energy was 1486.6 eV. Compositional analysis of the samples was carried out with an EHAX6293-H X-ray energy dispersion spectrometer (EDS). The current was set at 10 μA, and the voltage was 15 kV. The light absorption properties of the materials were studied by using a UV-3600 ultraviolet visible spectrophotometer (UV−vis). Photocatalytic degradation of

solutions was studied by using an Agilent 1290II-6460 high-performance liquid chromatograph (HPLC−MS). The specific surface area and pore diameter of the material were determined by a TRISTAR-3000 analyzer. The zeta potential was measured by a Malvern Nano ZS particle size analyzer.

2.4. Photocatalytic Experiments. A 500 W tungsten halogen lamp (λ > 420 nm) was used as the visible light source, and 100 mL (concentration 10 mg/L) of the TCH solution was added into the double-wall quartz reactor. The temperature of the reaction solutions was kept constant by the actions of the magnetic blender and the cooling system. The $Ag_2S-Bi_2WO_6$ composites (0.05 g) dispersed in the solution. The light source was turned off for the first 30 min so that the $Ag_2S-Bi_2WO_6$ composites and TCH could achieve adsorption equilibrium. The absorbance was measured at 357 nm by the DR6000 UV spectrophotometer.

3. RESULTS AND DISCUSSION

3.1. Material Characterization. *3.1.1. XRD Analysis.* The crystal phase and structure of the prepared photocatalyst were identified by X-ray diffraction, and the results are shown in Figure 1. The diffraction peaks of Bi_2WO_6 are strong and
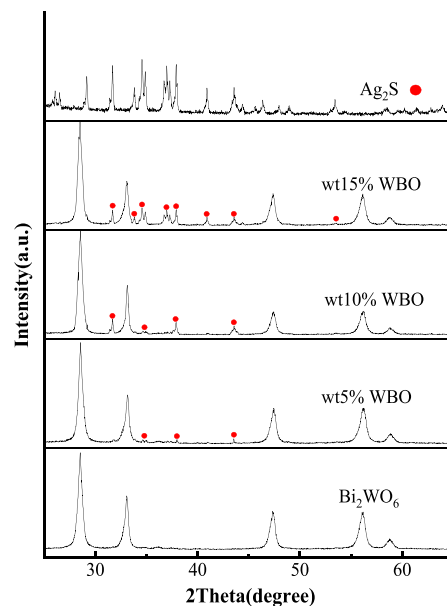

Figure 1. XRD of $Ag_2S-Bi_2WO_6$ composites.

sharp, indicating that the catalyst has excellent crystallinity. The diffraction peaks at 28.2, 32.7, 47.0, and 55.7° can be assigned to the (131), (200), (202), and (331) lattice planes of Bi_2WO_6 (JCPDS No. 39-0256).[23,24] The characteristic peaks at 31.82, 33.66, 34.74, and 36.81° correspond to the (120), (121), (112), and (022) lattice planes of Ag_2S (JCPDS No. 14-0072), which indicate the prepared monoclinic structure of Ag_2S.[25] Furthermore, the diffraction peak of the $Ag_2S-Bi_2WO_6$ composite does not shift significantly after loading Ag_2S, indicating that loading of Ag_2S particles does not change the lattice structure of Bi_2WO_6 but is located on its surface.[26] As the content of Ag_2S continues to decrease, the diffraction peaks of Ag_2S are not obvious, the reason for the doping amount of Ag_2S was low and the particles were small and highly dispersed.[27,28]
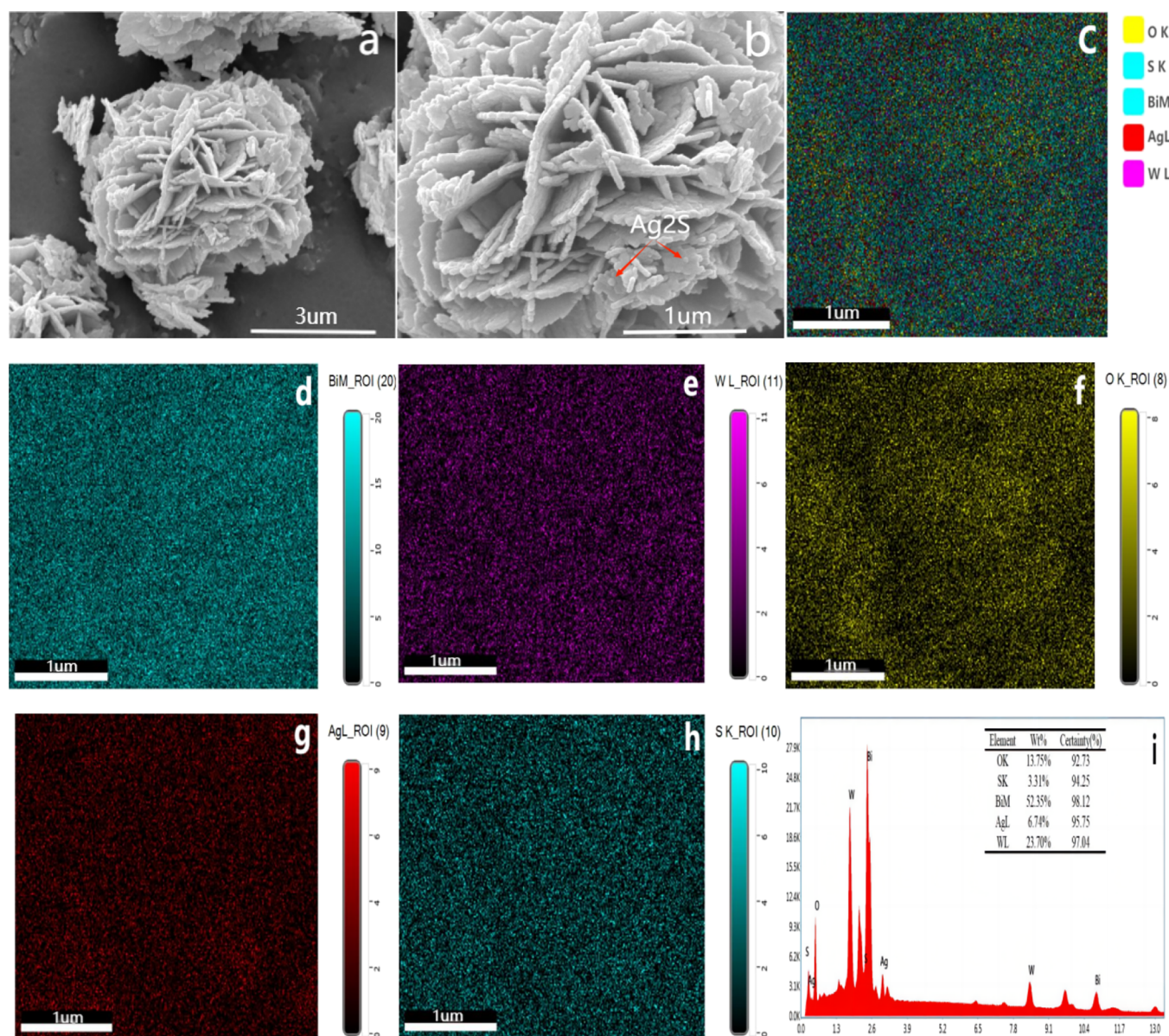
Figure 2. (a, b) SEM and (c−i) EDS of wt 10% BWO.

3.1.2. SEM and EDS Analysis. From the inspection of the SEM analysis for the morphology and composition of wt 10% BWO (Figure 2a,b), it can be seen that Bi_2WO_6 has a three-dimensional flower-shaped structure with a diameter of about 3 μm, with a more mesoporous structure and a large specific surface area and with Ag_2S being attached to its surface. Using EDS, the elemental composition of the sample was determined, and it can be seen that the wt 10% BWO contained W, Bi, O, Ag, and S.

3.1.3. XPS Analysis. The chemical bonding form of Bi_2WO_6 and wt 10% BWO was analyzed by XPS, with the binding energy for the spectrum being calibrated using C 1s (284.62 eV). Figure 3a shows the full spectrum of Bi_2WO_6, in which the binding energies of W, B, and O are clearly visible; there are no other elements. In Figure 3b,c, it can be seen that the binding energies at 159.4 and 164.8 eV correspond to Bi $4f_{7/2}$ and Bi $4f_{5/2}$, respectively, which indicate that Bi exists as Bi^{3+} in Bi_2WO_6.[29,30] The binding energies at 35.2 and 37.3 eV can be attributed to W $4f_{7/2}$ and W $4f_{5/2}$, and W exists as W^{6+}.[31,32]

The binding energies of O 1s at 530.0 eV correspond to lattice oxygen (O−Bi and O−W); there is no other form of oxygen.[33] In summary, the prepared Bi_2WO_6 was a pure phase compound.

In comparison with the XPS of Bi_2WO_6, there are newly emerged S 2p and Ag 3d binding energies of wt 10% BWO, and the location of binding energies of Bi 4f and W 4f has shifted slightly (Figure 4b,c). Because Ag_2S surface modifies Bi_2WO_6, the electron cloud density for Bi and W changes, thus leading to a change in the electronic structure.[34] The position and strength of lattice oxygen (Figure 5d) did not change, indicating that Ag_2S bonded with Bi_2WO_6 through surface modification without change in the internal crystal structure. But the newly emerging binding energies of O 1s at 532.5 eV correspond to water species adsorbed on the surface of as-prepared sample, which is more conducive to the formation of hydroxyl radical and superoxide free radical.[35] As shown in Figure 4e, the binding energies at 161.4 and 162.5 eV can be identified as S $2p_{3/2}$ and S $2p_{1/2}$, which correspond to S^{2-}; the
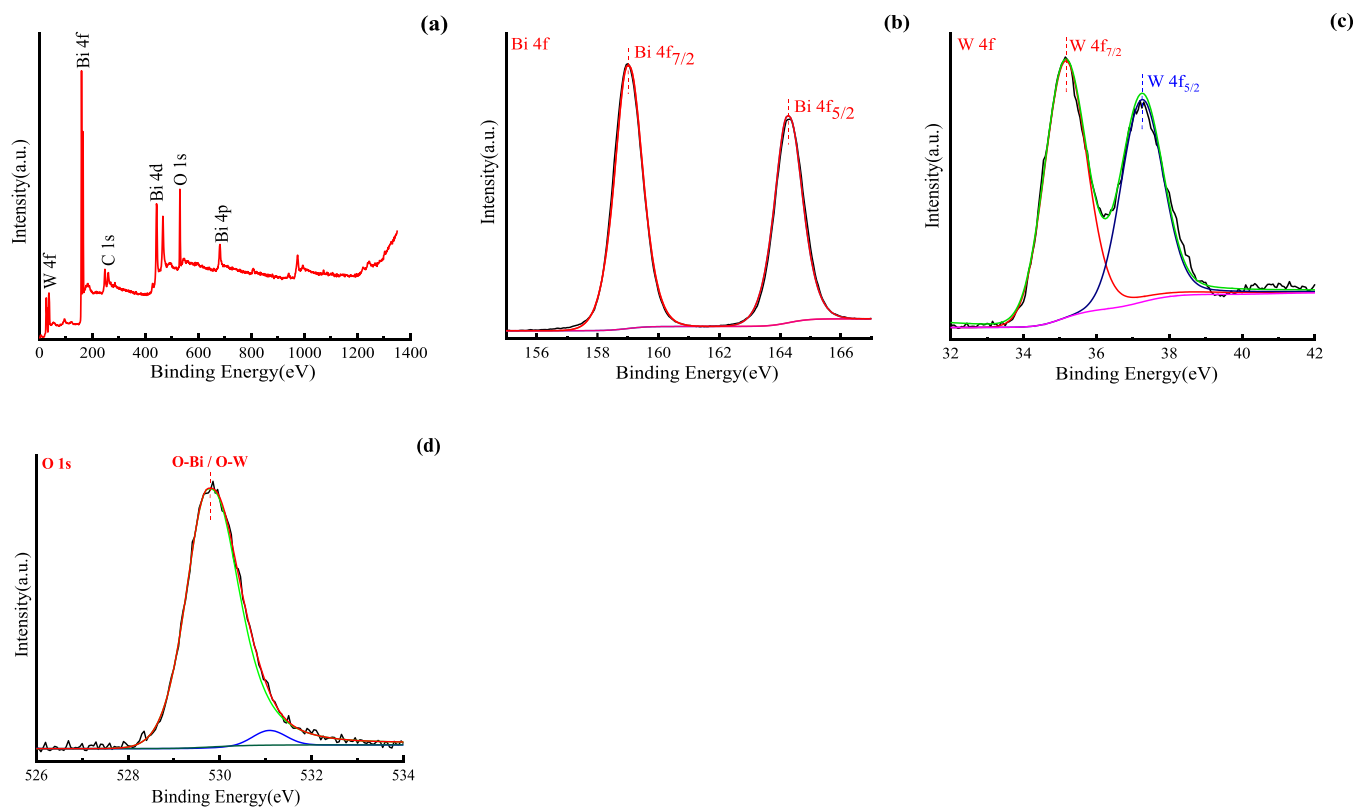
Figure 3. XPS of Bi_2WO_6. (a) Full spectrum, (b) Bi 4f, (c) W 4f, and (d)O 1s.
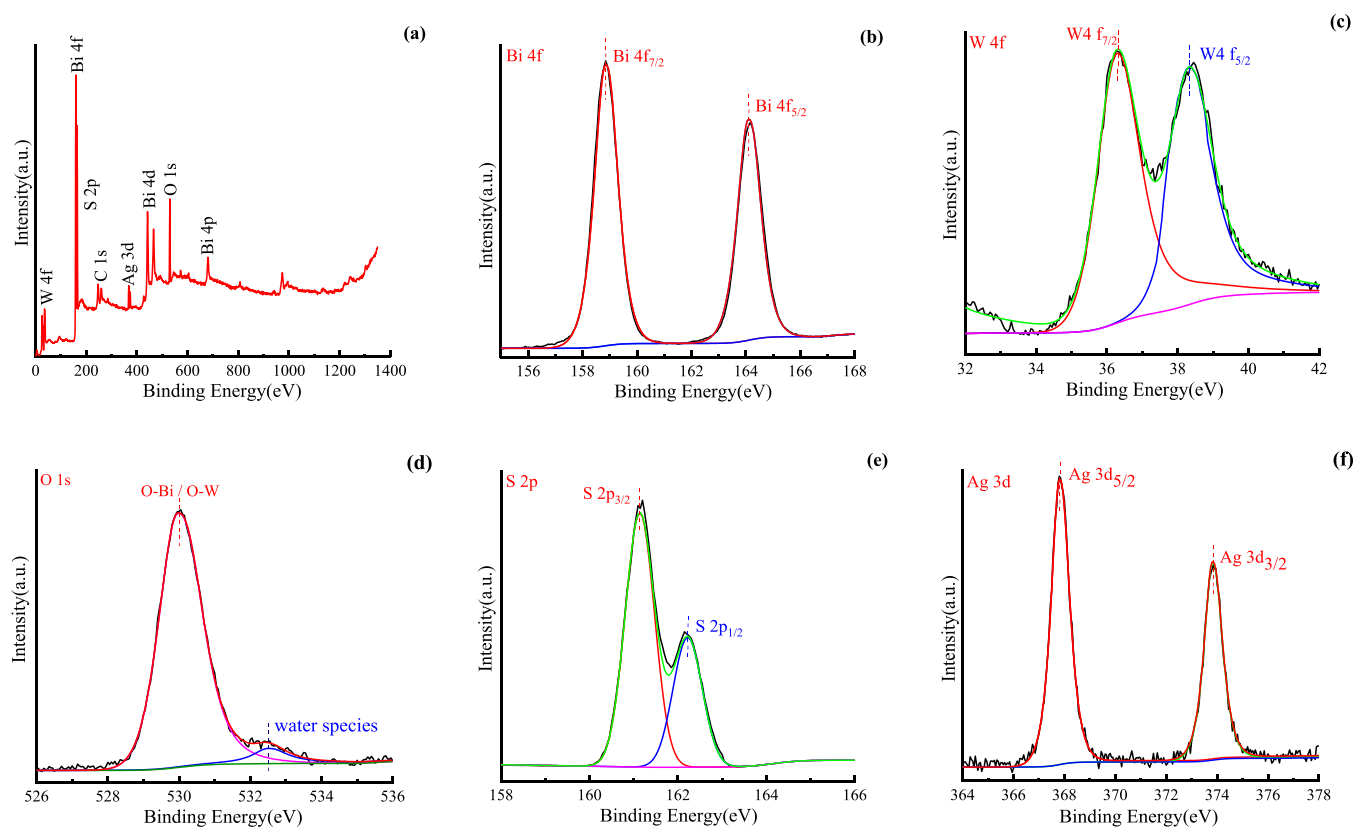

Figure 4. XPS of wt 10% BWO. (a) Full spectrum, (b) Bi 4f, (c) W 4f, (d) O 1s, (e) S 2p, and (f) Ag 3d.

binding energies at 367.8 and 373.9 eV (Figure 4f) correspond to Ag $3d_{5/2}$ and Ag $3d_{3/2}$, respectively.[25,36,37] According to

previous researches,[38,39] it can be clarified that the valence state of Ag in the composite is Ag^{1+}. In conclusion, the Ag_2S-
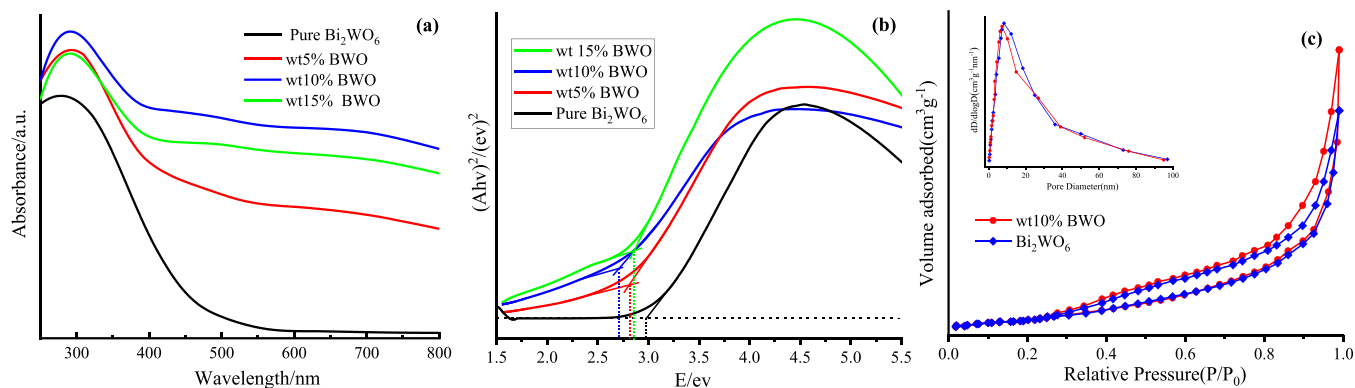
Figure 5. (a) UV−vis and (b) band gap energies of Bi_2WO_6 and the $Ag_2S−Bi_2WO_6$ composite. (c) N_2 adsorption−desorption isotherms of the synthetic samples.
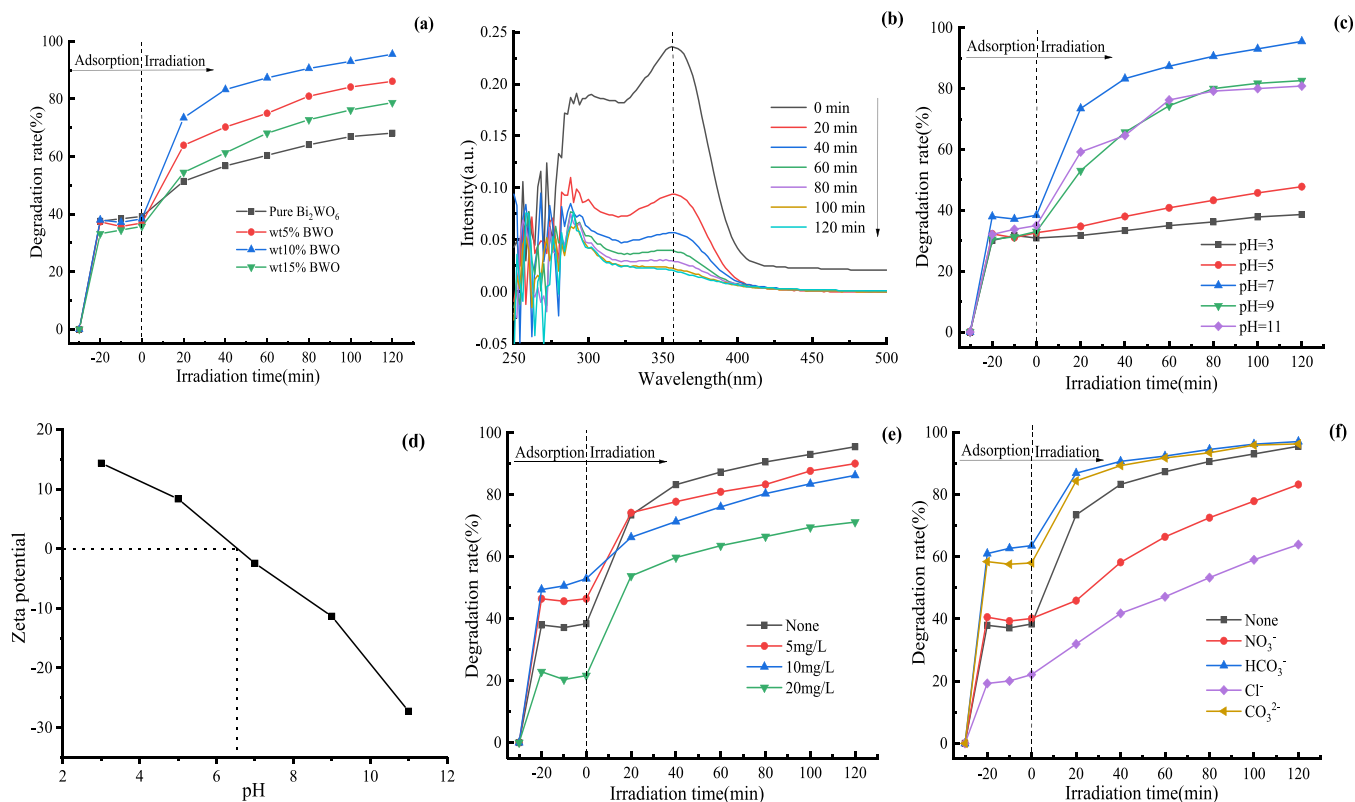

Figure 6. (a) Photocatalytic degradation of different weight ratios. (b) UV−vis spectrum. The effect of pH (c) and zeta potential of wt 10% BWO as a function of pH value (d). The effect of (e) humic acid and (f) inorganic anions.

Bi_2WO_6 composite was successfully combined by chemical energy.

3.1.4. UV−Vis and BET analysis. The wavelength range and intensity of absorption of visible light by a semiconductor play fundamental roles in photocatalytic oxidation reactions. Figure 5a shows the photosensitivity of $B_{i2}WO_6$ and $Ag_2S−Bi_2WO_6$ composites to visible light. Bi_2WO_6 absorbs radiation from the ultraviolet light to the visible; the absorption edge is located at about 460 nm, and there is no absorption after 550 nm, which is almost consistent with the results of recent literature.[40,41] The $Ag_2S−Bi_2WO_6$ composite absorption boundary has clearly red-shifted to about 550 nm, and there is still strong light absorption, but this extends to about 800 nm. The wt 10% BWO has the best visible light response and absorption range, conducive to the enhancement of photocatalytic activity.[42,43]

Figure 6b shows the forbidden bandwidths corresponding to Bi_2WO_6 that occur at about 2.96 eV, whereas those for the wt 5%, wt 10%, and wt 15% BWO are about 2.78, 2.68 and 2.82 eV, respectively.[44]

N_2 adsorption−desorption measurements are performed to investigate the BET surface areas and pore sizes of Bi_2WO_6 and wt 10% BWO. As shown in Figure 5c, both of the hysteresis loops of measured isotherms for Bi_2WO_6 and wt 10% BWO can be identified as typical type IV curves with an H3 hysteresis loop, which denoted the presence of a slit-like mesoporous structure.[45] The BET surface areas of Bi_2WO_6 and $Ag_2S−Bi_2WO_6$ are 56.39 and 62.47 m^2/g, respectively. After Ag_2S is added, the surface of Bi_2WO_6 is enlarged, indicating that more active sites are provided for the removal of contaminated matter. However, the pore size of wt 10%
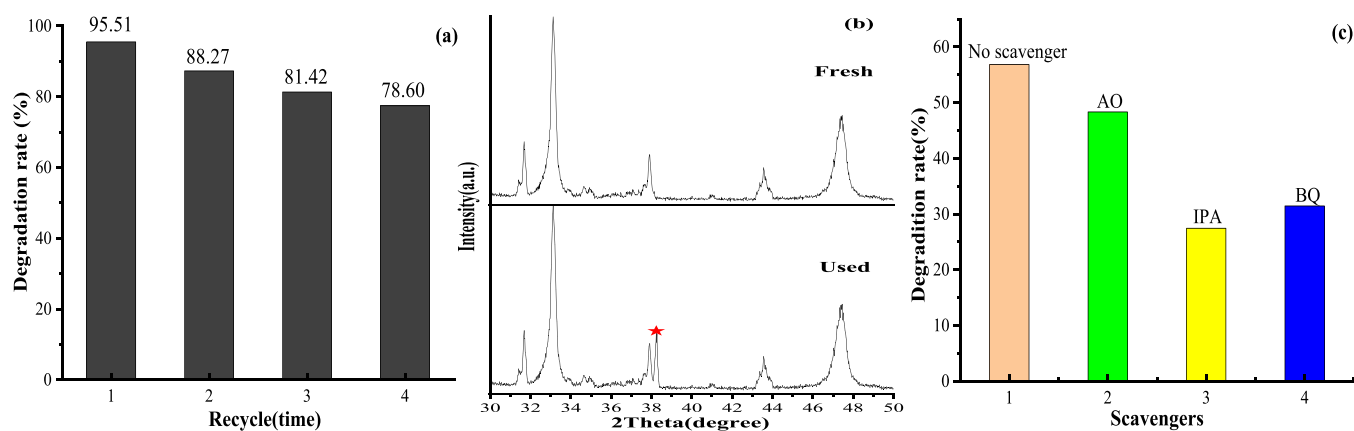
Figure 7. (a) Repeatability experiment, (b) XRD of the composite after repeated experiments, and (c) free radical trapping experiment.

BWO (8.82 nm) is smaller than that of Bi_2WO_6 (10.25 nm), which may be the reason that Ag_2S fills the Bi_2WO_6 hole. The suitable surface area and pore structure contribute to higher photocatalytic activity.

3.2. Photocatalytic Degradation Experiments.

3.2.1. Degradation of Tetracycline. As shown in Figure 6a, the degradation rate of Bi_2WO_6 was 68.16% within 150 min and was mainly attributed to the multilevel void structure that had a strong adsorption capacity. The photocatalytic property of $Ag_2S-Bi_2WO_6$ increased significantly and not only had a higher surface area but also provided more active sites.[46−50] The results showed that wt 10% BWO had the best photocatalytic efficiency, and the degradation rate of TCH was 95.51% within 150 min. The reason was that the composite inhibited the photogenerated electron−hole recombination.[51] The photocatalytic efficiency of wt 15% BWO decreased, and the effect was mainly reflected in the photocatalytic stage rather than adsorption. The reason for this is that the adhesion of excessive black Ag_2S on the surface of Bi_2WO_6 led to the shielding of the active site on the surface of the photocatalyst, which weakened the transmission performance of the incident light and affected the absorption of visible light by the composite.[52−54]

The UV−vis spectrum (Figure 6b) shows that as the reaction proceeded, the intensity of the characteristic peak at 357 nm gradually decreased. This result indicated that TCH was degraded, and the stable four-ring structure of TCH was destroyed by oxidation, gradually decomposing into small molecules.

3.2.2. The Effect of pH. pH is an extremely important parameter in wastewater treatment, which can be affected by changing the surface adsorption capacity of the catalyst or the hydrolytic form of the pollutants.[55,56] As the pH was increased from 3 to 11, degradation at first increased and then decreased (Figure 6c). The degradation rate was less than 40% at pH 3, whereas the value was more than 90% at pH 7.

The photocatalytic oxidation reaction process occurs mainly on the surface of the photocatalyst, so a composite that can effectively adsorb the TCH is a prerequisite for the photocatalytic reaction.[57,58] The pH directly affects the hydrolyzed form of the target pollutant. TCH exists mainly in the form of cations (TCH_3^+),[59] zwitterions $(TCH_2^\pm)$, anions (TCH^-), and bianions (TC_2^-) for pH conditions that are lower than 3.3, between 3.3 and 7.7, between 7.7 and 9.7, and beyond 9.7, respectively.[60,61] The variation of the zeta potential of wt 10% BWO with pH value is shown in Figure 6d.

When pH is less than 6.5, wt 10%BWO is positively charged, and when pH is greater than 6.5, it is negatively charged. Therefore, when pH is less than 3.3 or greater than 7.7, wt 10% BWO and TCH both carry the same charge on the surface and should repel each other, thus reducing the adsorption amount. However, with change of pH, the adsorption capacity of wt 10% BWO does not change significantly, indicating that surface electrostatic forces play no major role. It has been found that TCHs in the anionic state (TCH^-, TC_2^-) have a higher electron density than those in the cationic state (TCH_3^+) and hence are more likely to be attacked by active substances; it indicates that TCH is more easily degraded under neutral conditions.[62] In summary, pH seriously affects the photocatalytic property but has no effect on the adsorption of the composite.

3.2.3. The Effect of Humic Acid. Humic acid (HA) occurs extensively in soil, natural water bodies, and all sewage and has a great impact on the forms and migration performance of TCH.[63,64] The experimental results (Figure 6e) revealed that when the HA concentration increased from 0 to 20 mg/L, the degradation rate was severely inhibited in the photocatalytic stage. HA can act as a photosensitizer to promote the production of •OH and •O_2^-, thus improving the degradation rate of TCH. However, it will also be a competitive reaction with TCH for active substances or become a quenching agent reducing the content of active substances, thus inhibiting the photocatalytic efficiency.[65,66] In this experiment, the inhibitory effect was stronger than the promoting effect of HA, but HA at an appropriate concentration can accelerate the adsorption of composite catalyst.[67]

3.2.4. The Effect of Inorganic anions. Inorganic anions exist widely in wastewater and have variable effects on TCH.[68,69] The results are shown in Figure 6f. CO_3^{2-} and HCO_3^- improved the degradation rate of TCH within 150 min because CO_3^{2-} and HCO_3 will be hydrolyzed to CO_3^- $(E_0 = 1.78$ V, pH = 7) (eqs 1, 2) so that the CO_3^- can attack electron-rich groups such as phenols and nitrogen-containing compounds by means of electron transfer or hydrogen extraction, whereas the electron-rich groups such as phenol groups and dimethylammonium groups in the TCH structure become a priority as objects of destruction, thus accelerating the decomposition of TCH.[70,71] NO_3^- will consume h^+ to generate sparsely NO_2^-• and •O_2^-, which then further react with water to generate •OH, but with the addition of NO_3^-, the degradation rate was minimally affected, which suggests that the main active substances were the •O_2^- or •OH rather

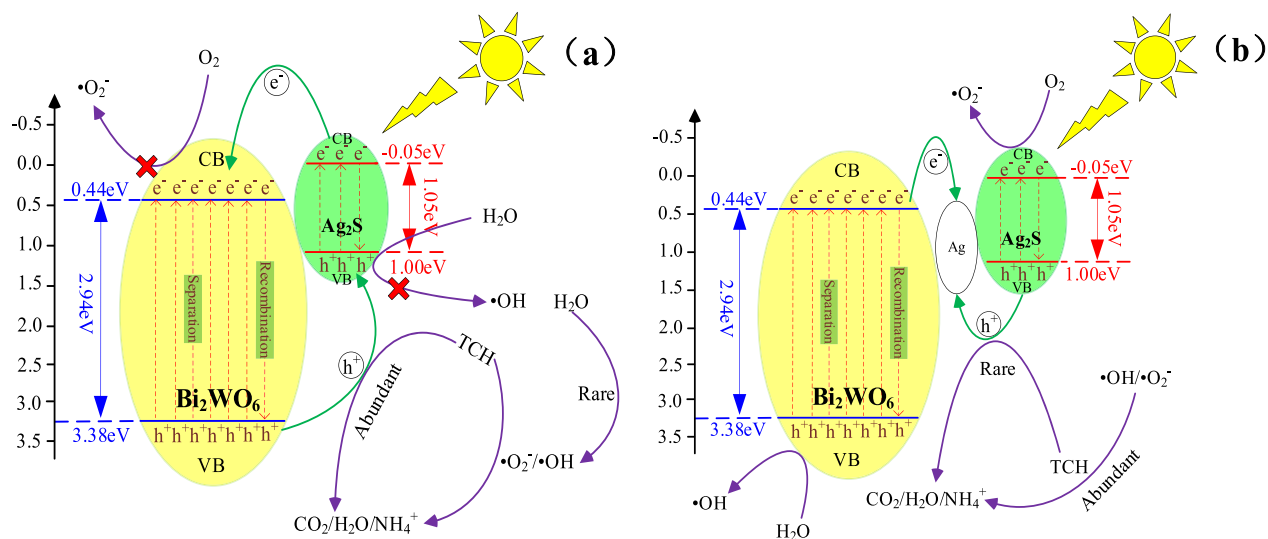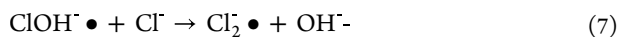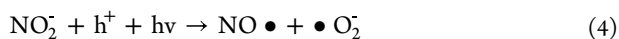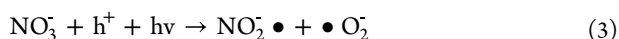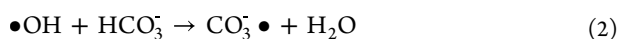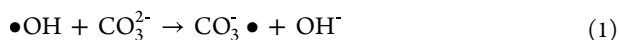**Figure 8.** Dual semiconductor systems' mechanism of the $Ag_2S-Bi_2WO_6$ composite.

than h^+[72] (eqs 3 − 5). Cl^- can seriously affect the degradation rate of TCH because the Cl^- consumes •OH to form low reactive $ClOH^-•$ and $Cl_2^-•$ (eqs 6 and 7), which further inferred that •OH was one of the main active substances.

$$•OH + CO_3^{2-} \rightarrow CO_3^- • + OH^- \tag{1}$$

$$•OH + HCO_3^- \rightarrow CO_3^- • + H_2O \tag{2}$$

$$NO_3^- + h^+ + hv \rightarrow NO_2 • + • O_2^- \tag{3}$$

$$NO_2^- + h^+ + hv \rightarrow NO • + • O_2^- \tag{4}$$

$$•O_2^- + H_2O \rightarrow •OH + OH^- \tag{5}$$

$$Cl^- + •OH \leftrightarrow ClOH^- • \tag{6}$$

$$ClOH^- • + Cl^- \rightarrow Cl_2^- • + OH^{-} \tag{7}$$

3.3. Stability of the Composite. The reuse rate of the composite is an important parameter and typically can serve as a measure of the stability of the catalyst.[73,74] After four cycles of experiments, the degradation rates of TCH decreased to 78.60% (Figure 7a). The samples collected after four cycles were tested by XRD, and the characterization results are shown in Figure 7b. The new diffraction peak at 38.25° corresponds to Ag^0.[75] Ag_2S is corroded by light, and part of Ag^+ is restored to Ag^0, which covers part of the active site; this is the main reason for the continuous decline of photocatalytic activity with repeated experiments.[76,77]

3.4. Free Radical Trapping Experiment. To study the mechanism of the photocatalytic process, the main active species in the photocatalytic degradation of TCH were identified by conducting a free radical capture experiment. Isopropyl alcohol (IPA), p-benzoquinone (BQ), and ammonium oxalate (AO) were used as quenching agents for the hydroxyl radical (•OH), the superoxide radical (•O_2^-), and the photogenic hole (h^+), respectively.[78,79] Except for the dosage of BQ that was 1 mmol/L, the other quenchers were all 10 mmol/L. As shown in Figure 7c, the addition of AO had little effect on the photocatalytic degradation rate, indicating that h^+ was not the main active pollutant in this experiment; this finding is consistent with the analysis results for the inorganic anions. In contrast, the degradation rates of TCH

decreased sharply after the addition of IPA, indicating that •OH was the main active substance in the reaction system, which is the reason why the photocatalytic degradation rate dropped sharply after the addition of Cl^-. BQ also had a great effect on the degradation rate, indicating that O_2^- was also one of the active substances.

3.5. Analysis of Photocatalytic Mechanism. The conduction band (CB) and valence band (VB) edges of Bi_2WO_6 and Ag_2S can be calculated by the Mulliken empirical formula (eqs 8 and 9)

$$E_{VB} = X \text{-} E^e + 0.5E_g \tag{8}$$

$$E_{CB} = E_{VB} \text{-} E_g \tag{9}$$

where E_{VB} and E_{CB} are the potentials at the top of the valence band and the bottom of the conduction band relative to the standard (H_2) electrode potential, respectively; X is the electronegativity of the semiconductor; E^e is the energy of the free electron (about 4.5 eV); and E_g is the band gap width of the semiconductor.

The electronegativity of Ag_2S is 4.97 eV, and the band gap is about 1.05.[80] The E_{VB} values for Ag_2S and Bi_2WO_6 are 1.00 and 3.38 eV, and the E_{CB} values are −0.05 and 0.44 eV, respectively. In $Ag_2S-Bi_2WO_6$ composites, the separation of photoproduced electron−hole pairs follows the common separation mechanism that is usually observed in composite photocatalysts (Figure 8a). The conduction band of Bi_2WO_6 (0.44 eV vs NHE) is higher than the redox potential of O_2 (−0.046 eV vs NHE). Photocatalyzed electrons do not react with O_2 to form •O_2^-.[81] Similarly, the hole in the valence band of Ag_2S (1.00 eV vs NHE) will not react with H_2O (2.30 eV vs NHE) to form •OH. However, these findings contradict the results of the free radical trapping experiments.

Therefore, the "dual semiconductor systems consisting of Ag NPs" are proposed (Figure 8b).[82,83] Under visible light, part of Ag_2S is reduced into Ag NPs that become attached to the surface of the $Ag_2S-Bi_2WO_6$ composite, forming $Ag@Ag_2S-Bi_2WO_6$. Ag NPs have two roles in dual semiconductor systems, that is, as electronic mediators and photosensitizers, which depend on the optical response of the two semiconductors.[84,85] In this study, because Ag_2S and Bi_2WO_6 can be excited by visible light, the Ag NPs function merely as an
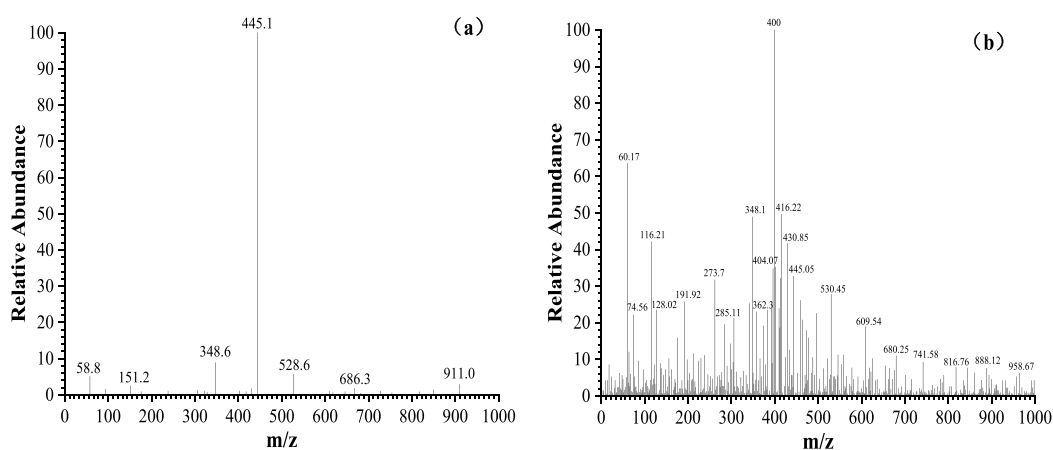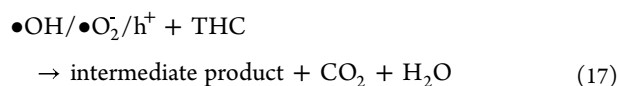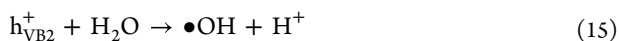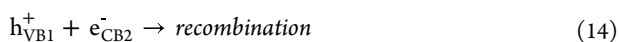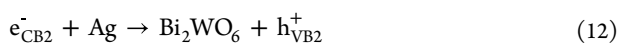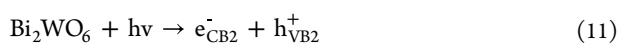
Figure 9. Mass spectra of tetracycline hydrochloride at (a) 0 and (b) 120 min.

electron transfer medium. Meanwhile, photonic absorption results in the excitation of Bi_2WO_6 and Ag_2S from their ground state to an excited state, electrons and holes are separated, and electrons in the conductive band of Bi_2WO_6 and the hole in valence band of Ag_2S rapidly combine through the Ag NPs. Results show that the photocatalytic electrons concentrated in the Ag_2S conduction band and the holes concentrated in the valence band of Bi_2WO_6, and this greatly accelerates the photogenerated electron−hole transfer and separation. The electrons in the conduction band of Ag_2S (−0.046 eV vs NHE) readily react with O_2 (2.30 eV vs NHE) to produce $\bullet O_2^-$, and the holes in the valence band of Bi_2WO_6 (0.49 eV vs NHE) can result in the oxidization of hydroxyl group surfaces or surface-bonded water molecules so that highly reactive and nonselective $\bullet OH$ (−0.046 eV vs NHE) can be obtained (eqs 10−17). TCH pollutant is attacked and decomposed into nontoxic substances by $\bullet OH$ and $\bullet O_2^-$. Therefore, the good photocatalytic performance of the "dual semiconductor systems consisting of Ag NPs" explains the reason why $\bullet OH$ and $\bullet O_2^-$ are the main active substances in this study.

$$Ag_2S + hv \rightarrow e_{CB1}^- + h_{VB1}^+ \tag{10}$$

$$Bi_2WO_6 + hv \rightarrow e_{CB2}^- + h_{VB2}^+ \tag{11}$$

$$e_{CB2}^- + Ag \rightarrow Bi_2WO_6 + h_{VB2}^+ \tag{12}$$

$$h_{VB1}^+ + Ag \rightarrow Ag_2S + e_{CB1}^- \tag{13}$$

$$h_{VB1}^+ + e_{CB2}^- \rightarrow recombination \tag{14}$$

$$h_{VB2}^+ + H_2O \rightarrow \bullet OH + H^+ \tag{15}$$

$$e_{CB1}^- + O_2 \rightarrow \bullet O_2^- \tag{16}$$

$$\bullet OH/\bullet O_2^-/h^+ + THC$$
$$\rightarrow intermediate\ product + CO_2 + H_2O \tag{17}$$

3.6. Possible Degradation Pathways of TCH. According to the photocatalytic reaction mechanism, the nature of degradation of TCH is the result of the strong oxidation of photocatalytically active substances. Figure 9a shows the mass spectrum of 0 min and m/z 445.1 that can be attributed to TCH because the HCl is readily removed by TCH in the water solubilization process and becomes TC.[86] Figure 9b shows the mass spectrum of 120 min, from which it can be seen that the

characteristic peak of TCH has decreased significantly, indicating that TCH in the reaction system has been degraded to other products. The degradation products mainly have characteristic peaks at 285, 343, 359, 400, 402, 416, and 431. It is speculated that there are two degradation pathways (Figure 10): First, TC loses the $-CONH_2$ to from **A** (m/z 402), then **A** loses the $-N(CH_3)_2$ to form **B** (m/z 359), and **C** (m/z 343) was formed by losing $-C=O$ of **B**. Finally, **C** loses $-CH_2CH(OH)CH_3$ to form **D** (m/z 285).[87,88] Second, TC breaks the low-energy N−C bond as a result of attack by active substances, thus losing the $N-CH_3$ and gaining intermediate **E** (m/z 431); then, **E** loses the $-NH$ to form **F** (m/z 416); when **F** loses the C−OH, intermediate **G** (m/z 400) is gained.[89]

These intermediates result in the production of a wide variety of small molecule organics of various structures through ring-opening reactions, central carbon cracking, or addition reactions. As the reaction continues, the intermediates will eventually be degraded into small molecules such as CO_2, H_2O and NH_4^+.

4. CONCLUSIONS

Three-dimensional flower-shaped Bi_2WO_6 and $Ag_2S-Bi_2WO_6$ composites were prepared by a hydrothermal procedure and precipitation methods. According to the characterization and photocatalytic degradation experiments, the photocatalytic performance was demonstrated to be optimal when the weight ratios of the composites were 10%, and the degradation rate of TCH reached 95.51%, which was 27.35% higher than that for the pure Bi_2WO_6. The reason for this was that the dual semiconductor systems formed by Ag_2S and Bi_2WO_6 reduce the photogenic electron−hole binding rate, thus producing a large number of highly oxidizing $\bullet OH$ and $\bullet O_2^-$ species. However, at neutral pH, the degradation efficiency was found to be the best, and the HA concentration correlated inversely with the degradation rate. Different inorganic anions were found to promote or inhibit the degradation efficiency of TCH, and the degradation rate was affected mainly by changing the content of main active substances. Because different factors will affect the degradation performance of the $Ag_2S-Bi_2WO_6$ composite, it is suitable for the advanced treatment of industrial wastewater. According to mass spectrometry analysis, the degradation pathway of TCH proceeds via the open-loop decomposition of the benzene ring structure, which would eventually cause substrate degradation into small inorganic molecules such as CO_2, H_2O, and NH_4^+. It is hoped that this
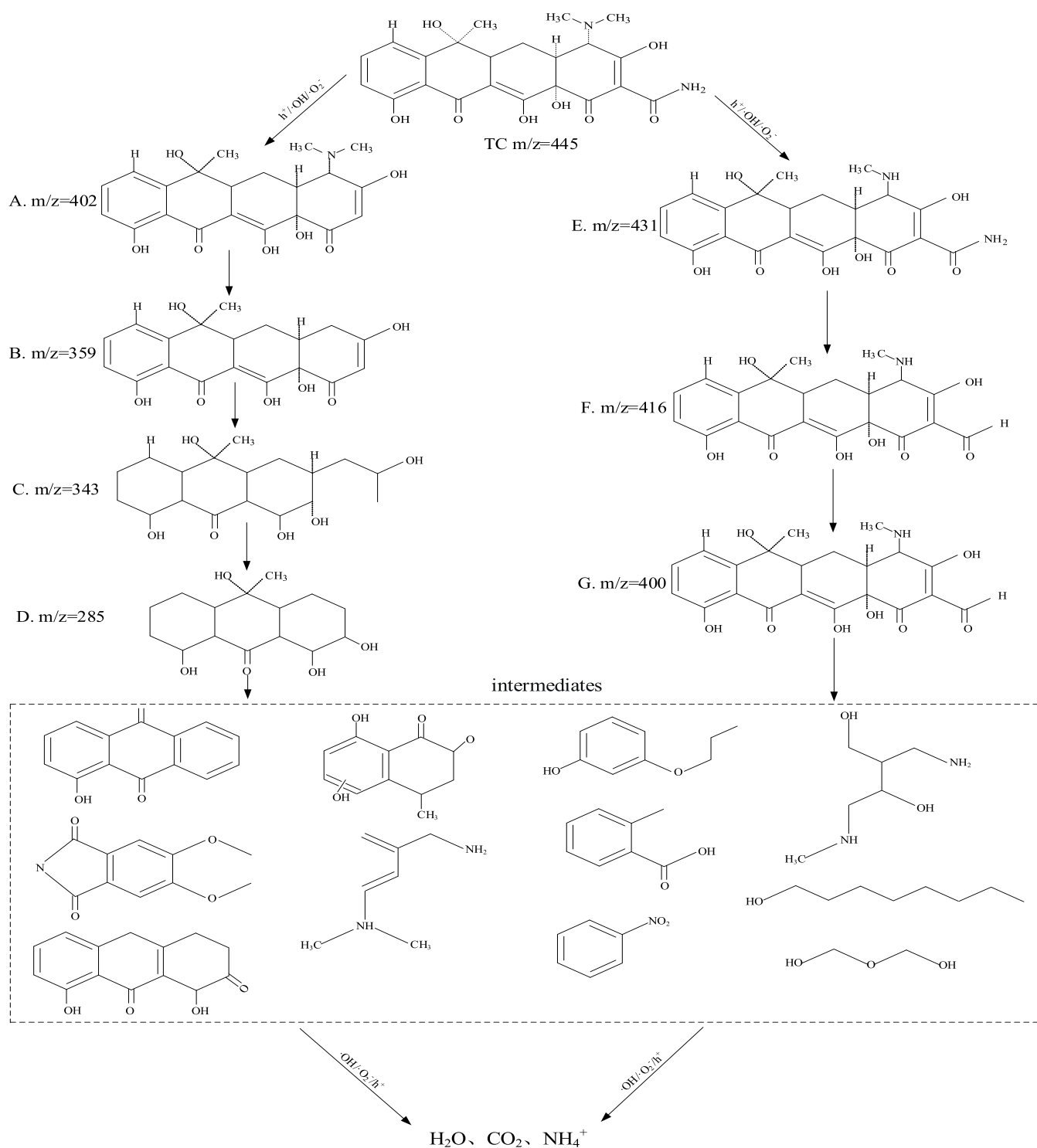
Figure 10. Proposed photocatalytic degradation pathway of TCH.

work can provide a benchmark for the design and preparation of a new dual semiconductor system photocatalyst to realize a more efficient, economical, and green application of photocatalysis in the field of water treatment.

■ AUTHOR INFORMATION

Corresponding Author

Hengcan Dai − *College of Civil Engineering, Guizhou University, Guiyang, Guizhou 550025, PR China;*
ⓘ orcid.org/0009-0004-4241-6511; Email: dhengcan@163.com

Authors

Xiaoliang Yang − *POWERCHINA Guizhou Electric Power Engineering Co., Ltd., Guiyang, Guizhou 550025, PR China*
Fei Tang − *College of Civil Engineering, Guizhou University, Guiyang, Guizhou 550025, PR China*

Complete contact information is available at:
https://pubs.acs.org/10.1021/acsomega.3c05386

■ REFERENCES

(1) Diao, Z.-H.; Huang, S.-T.; Chen, X.; Zou, M.-Y.; Liu, H.; Guo, P.-R.; Kong, L.-J.; Chu, W. Peroxymonosulfate-assisted photocatalytic degradation of antibiotic norfloxacin by a calcium-based Ag_3PO_4 composite in water: Reactivity, products and mechanism. *Journal of Cleaner Production* **2022**, *330*, No. 129806.

(2) Li, S.; Wang, C.; Liu, Y.; Cai, M.; Wang, Y.; Zhang, H.; Guo, Y.; Zhao, W.; Wang, Z.; Chen, X. Photocatalytic degradation of tetracycline antibiotic by a novel $Bi_2Sn_2O_7/Bi_2MoO_6$ S-scheme heterojunction: Performance, mechanism insight and toxicity assessment. *Chem. Eng. J.* **2022**, *429*, No. 132519.

(3) Liu, T.; Wang, C.; Ding, C.; Wang, W.; Wang, B.; Wang, M.; Zhang, J. The improved photocatalytic antibiotic removal performance achieved on Ir/WO2.72 photocatalysts. *Colloids Surf., A* **2022**, *645*, No. 128891.

(4) Nguyen, T. H. A.; Le, V. T.; Doan, V.-D.; Tran, A. V.; Nguyen, V. C.; Nguyen, A.-T.; Vasseghian, Y. Green synthesis of Nb-doped ZnO nanocomposite for photocatalytic degradation of tetracycline antibiotic under visible light. *Mater. Lett.* **2022**, *308*, No. 131129.

(5) Hu, X.; Yu, Y.; Chen, D.; Xu, W.; Fang, J.; Liu, Z.; Li, R.; Yao, L.; Qin, J.; Fang, Z. Anatase/Rutile homojunction quantum dots anchored on g-C_3N_4 nanosheets for antibiotics degradation in seawater matrice via coupled adsorption-photocatalysis: Mechanism insight and toxicity evaluation. *Chem. Eng. J.* **2022**, *432*, 134375.

(6) Xie, Y.; Yu, Y.; Xie, H.; Huang, F.; Hughes, T. C. 3D-printed heterogeneous Cu_2O monoliths: Reusable supports for Antibiotic Treatmentantibiotic treatment of wastewater. *J. Hazard. Mater.* **2022**, *2*, No. 129170.

(7) Zhang, X.; Xu, B.; Wang, S.; Li, X.; Liu, B.; Xu, Y.; Yu, P.; Sun, Y.J.J.o.H.M. High-density dispersion of CuNx sites for H_2O_2 activation toward enhanced Photo-Fenton performance in antibiotic contaminant degradation. *J. Hazard. Mater.* **2022**, *423*, 127039.

(8) Jing, L.; Xu, Y.; Liu, J.; Zhou, M.; Xu, H.; Xie, M.; Li, H.; Xie, J. Direct Z-scheme red carbon nitride/rod-like lanthanum vanadate composites with enhanced photodegradation of antibiotic contaminants. *Appl. Catal. B: Environ.* **2020**, *277*, No. 119245.

(9) Wieckowska, A.; Jablonowska, E.; Dzwonek, M.; Jaskolowski, M.; Bilewicz, R. J. C. Tailored Lipid Monolayers Doped with Gold Nanoclusters: Surface Studies and Electrochemistry of Hybrid-film-covered Electrodes. *ChemElectroChem.* **2022**, *9*, No. e202101367, DOI: 10.1002/celc.202101367.

(10) Balan, B.; Xavier, M. M.; Mathew, S. MoS_2-Based Nanocomposites for Photocatalytic Hydrogen Evolution and Carbon Dioxide Reduction. *ACS Omega* **2023**, *8*, 25649−25673.

(11) Pan, Y.; Abazari, R.; Yao, J.; Gao, J. Recent progress in 2D metal-organic framework photocatalysts: synthesis, photocatalytic mechanism and applications. *Journal of Physics: Energy* **2021**, *3*, No. 032010.

(12) Kalhorizadeh, T.; Dahrazma, B.; Zarghami, R.; Mirzababaei, S.; Kirillov, A. M.; Abazari, R. Quick removal of metronidazole from aqueous solutions using metal−organic frameworks. *New J. Chem.* **2022**, *46*, 9440−9450.

(13) Zhang, R.; Yu, J.; Zhang, T.; Zhao, C.; Han, Q.; Li, Y.; Liu, Y.; Zeng, K.; Cai, L.; Yang, Z.; et al. A novel snowflake dual Z-scheme $Cu_2S/$ RGO/ Bi_2WO_6 photocatalyst for the degradation of bisphenol A under visible light and its effect on crop growth. *Colloids Surf., A* **2022**, *641*, No. 128526.

(14) Wang, L.; Liu, Y.; Lin, Y.; Zhang, X.; Yu, Y.; Zhang, R. Z-scheme $Cu_2(OH)_3F$ nanosheets-decorated 3D Bi_2WO_6 heterojunction with an intimate hetero-surface contact through a hydrogen bond for enhanced photoinduced charge separation and transfer. *Chem. Eng. J.* **2022**, *427*, No. 131704.

(15) Zhang, R.; Jiang, J.; Zeng, K. Synthesis of Bi_2WO_6/g-C_3N_4 heterojunction on activated carbon fiber membrane as a thin-film photocatalyst for treating antibiotic wastewater. *Inorg. Chem. Commun.* **2022**, *140*, No. 109418.

(16) Danlian, Huang; Jing, Li; Guangming, Zeng; Wenjing, Xue; Journal, S. J. C. E. Facile construction of hierarchical flower-like Z-scheme $AgBr/Bi_2WO_6$ photocatalysts for effective removal of tetracycline: Degradation pathways and mechanism. *Chem. Eng. J.* **2019**, No. 121991, DOI: 10.1016/j.cej.2019.121991.

(17) Rao, F.; Liu, H.; Zhong, J.; Li, J. In-situ construction of $Bi_2WO_6/ZnWO_4$ heterojunctions with enhanced photocatalytic performance toward RhB degradation. *Mater. Lett.* **2022**, *312*, 131707.

(18) Tian, Q.; Ouyang, W.; Wang, Y.; Ji, Y.J.F.M.L. One-step route for Z-scheme $Al_2(WO_4)_3/Bi_2WO_6$ heterojunction toward superior photoelectric and photocatalytic performance. *Funct. Mater. Lett.* **2022**, *15*, 2251008 DOI: 10.1142/S1793604722510080.

(19) Xue, W.; Peng, Z.; Huang, D.; Zen, G.; Weng, X.; Deng, R; Yang, Y.; Yan, X In situ synthesis of visible-light-driven Z-scheme AgI/Bi2WO6 heterojunction photocatalysts with enhanced photocatalytic activity. *Ceram. Int.* **2019**, *45*, 6340 DOI: 10.1016/j.ceramint.2018.12.119.

(20) Fan, Z.; Luan, J.; Zhu, C.; Liu, F.J.M.R.B. Depositing Ag_2S quantum dots as electron mediators in SnS_2/g-C_3N_4 nanosheet composites for constructing Z-scheme heterojunction with enhanced photocatalytic performance. *Mater. Res. Bull.* **2021**, *133*, No. 111045.

(21) John Peter, I.; Ramachandran, K.; Vijaya, S.; Anandan, S.; Nithiananthi, P. Effect of Phosphor on the efficiency of $TiO_2/CdS/Ag_2S$ heterostructure based Solar Cells. *Mater. Lett.* **2019**, *240*, 291−294.

(22) Shi, E.; ZhenlanWang, WenjingXu; YiZhang, YihengYang; XuezhiLiu, QianZeng; TaoSong, ShuangJiang; YinzhiLi, LingxiangyuSharma; Virender, K. Ag_2S-doped core-shell nanostructures of $Fe_3O_4@Ag_3PO_4$ ultrathin film: Major role of hole in rapid degradation of pollutants under visible light irradiation. *Chem. Eng. J.* **2019**, *366*, 123 DOI: 10.1016/j.cej.2019.02.018.

(23) Chen, Y.; Zhang, F.; Guan, S.; Shi, W.; Wang, X.; Huang, C.; Chen, Q. Visible light degradation of tetracycline by hierarchical nanoflower structured fluorine-doped Bi_2WO_6. *Mater. Sci. Semicond. Process.* **2022**, *140*, 106385.

(24) Shangguan, X. Y.; Fang, B. L.; Xu, C. X.; Tan, Y.; Chen, Y. G.; Xia, Z. J.; Chen, W. Fabrication of direct Z-scheme $FeIn_2S_4/Bi_2WO_6$ hierarchical heterostructures with enhanced photocatalytic activity for tetracycline hydrochloride photodagradation. *Ceram. Int.* **2021**, *47*, 6318−6328.

(25) Shen, X.; Yang, J.; Zheng, T.; Wang, Q.; Zhuang, H.; Zheng, R.; Shan, S.; Li, S. Plasmonic p-n heterojunction of $Ag/Ag_2S/Ag_2MoO_4$ with enhanced Vis-NIR photocatalytic activity for purifying wastewater. *Sep. Purif. Technol.* **2020**, *251*, No. 117347.

(26) Wan, W.; Yang, X.; Du, M.; Shi, Y.; Wang, J.; Wang, L.; Chin, Y.; Liu, H.; Zhang, P. One-dimensional ternary $Ag@Ag_2S@C$ nanocable with plasmon-enhanced photocatalytic performance. *Molecular Catalysis* **2021**, *505*, No. 111531.

(27) Zhao, X.; Yang, H.; Li, R.; Cui, Z.; Liu, X. Synthesis of heterojunction photocatalysts composed of Ag_2S quantum dots combined with $Bi_4Ti_3O_{12}$ nanosheets for the degradation of dyes. *Environ. Sci. Pollut. Res.* **2019**, *26*, 5524−5538.

(28) Di, L.; Yang, H.; Xian, T.; Liu, X.; Chen, X. Photocatalytic and Photo-Fenton Catalytic Degradation Activities of Z-Scheme $Ag_2S/$ BiFeO Heterojunction Composites under Visible-Light Irradiation. *Nanomaterials* **2019**, *9*, 399 DOI: 10.3390/nano9030399.

(29) Wang, T.; Feng, C.; Liu, J.; Wang, D.; Hu, H.; Hu, J.; Chen, Z.; Xue, G. Bi_2WO_6 hollow microspheres with high specific surface area and oxygen vacancies for efficient photocatalysis N_2 fixation. *Chem. Eng. J.* **2021**, *414*, No. 128827.

(30) Qiang, Z.; Liu, X.; Li, F.; Li, T.; Zhang, M.; Singh, H.; Huttula, M.; Cao, W. Iodine doped Z-scheme $Bi_2O_2CO_3/Bi_2WO_6$ photo-

catalysts: Facile synthesis, efficient visible light photocatalysis, and photocatalytic mechanism. *Chem. Eng. J.* **2021**, *403*, No. 126327.

(31) Wang, Y.; Liu, L.; Zhang, J.; Zhang, W.; Yao, W.; Jiang, G. NiFe...ayered Double Hydroxide/Vertical Bi$_2$WO$_6$ Nanoplate Arrays with Oriented {001} Facets Supported on ITO Glass: Improved Photoelectrocatalytic Activity and Mechanism Insight. *ChemCatChem* **2021**, *13*, 3414−3420.

(32) Adhikari, S.; Selvaraj, S.; Kim, D. H. Construction of heterojunction photoelectrode via atomic layer deposition of Fe$_2$O$_3$ on Bi$_2$WO$_6$ for highly efficient photoelectrochemical sensing and degradation of tetracycline. *Applied Catalysis B: Environmental* **2019**, *244*, 11−24.

(33) Mao, W.; Zhang, L.; Liu, Y.; Wang, T.; Bai, Y.; Guan, Y. J. C. Facile assembled N, S-codoped corn straw biochar loaded Bi$_2$WO$_6$ with the enhanced electron-rich feature for the efficient photocatalytic removal of ciprofloxacin and Cr(VI). *Chemosphere* **2021**, *263*, 127988.

(34) Zhang, Y.; Zhao, Y.; Xiong, Z.; Gao, T.; Gong, B.; Liu, P.; Liu, J.; Zhang, J. Elemental mercury removal by I-doped Bi$_2$WO$_6$ with remarkable visible-light-driven photocatalytic oxidation. *App. Catal. B: Environ.* **2021**, *282*, No. 119534.

(35) Shin, J.; Heo, J. N.; Do, J. Y.; Kim, Y. I.; Yoon, S. J.; Kim, Y. S.; Kang, M. Effective charge separation in rGO/NiWO$_4$@Au photocatalyst for efficient CO$_2$ reduction under visible light. *J. Ind. Eng. Chem.* **2020**, *81*, 427−439.

(36) Liang, T.-Y.; Chan, S.-J.; Patra, A. S.; Hsieh, P.-L.; Chen, Y.-A.; Ma, H.-H.; Huang, M. H. Inactive Cu$_2$O Cubes Become Highly Photocatalytically Active with Ag$_2$S Deposition. *ACS Appl. Mater. Interfaces* **2021**, *13*, 11515−11523.

(37) Zeng, Y.; Lu, D.; Kondamareddy, K. K.; Wang, H.; Wu, Q.; Fan, H.; Wang, Q.; Zhang, B.; Xie, L.; Zhang, Y.J.J.o.A. Enhanced visible light photocatalysis and mechanism insight for novel Z-scheme MoS$_2$/Ag$_2$S/AgVOx ternary heterostructure with fast interfacial charges transfer. *J. Alloys Compd.* **2022**, *908*, 164642.

(38) Xue, B.; Jiang, H.-Y.; Sun, T.; Mao, F.; Ma, C.-C.; Wu, J.-K. Microwave-assisted one-step rapid synthesis of ternary Ag/Ag$_2$S/g-C$_3$N$_4$ heterojunction photocatalysts for improved visible-light induced photodegradation of organic pollutant. *J. Photochem. Photobiol., A* **2018**, *353*, 557−563.

(39) Dong, X.; Wang, S.; Wu, Q.; Liu, K.; Kong, F.; Liu, J. Co-catalyst boosted photocatalytic hydrogen production driven by visible-light over g-C$_3$N$_4$: The synergistic effect between Ag and Ag$_2$S. *J. Alloys Compd.* **2021**, *875*, No. 160032.

(40) Yuan, X.; Shen, D.; Zhang, Q.; Zou, H.; Liu, Z.; Peng, F. Z-scheme Bi$_2$WO$_6$/CuBi$_2$O$_4$ heterojunction mediated by interfacial electric field for efficient visible-light photocatalytic degradation of tetracycline. *Chem. Eng. J.* **2019**, *369*, 292−301.

(41) Hua, C.; Wang, J.; Dong, X.; Wang, Y.; Zheng, N.; Xue, M.; Zhang, X. In situ plasmonic Bi grown on I− doped Bi$_2$WO$_6$ for enhanced visible-light-driven photocatalysis to mineralize diverse refractory organic pollutants. *Sep. Purif. Technol.* **2020**, *250*, No. 117119.

(42) Hu, X.; Ma, Q.; Wang, X.; Yang, Y.; Liu, N.; Zhang, C.; Kawazoe, N.; Chen, G.; Yang, Y. Layered Ag/Ag$_2$O/BiPO4/Bi$_2$WO$_6$ heterostructures by two-step method for enhanced photocatalysis. *J. Catal.* **2020**, *387*, 28−38.

(43) Li, J.; Zhao, Y.; Xia, M.; An, H.; Bai, H.; Wei, J.; Yang, B.; Yang, G. Highly efficient charge transfer at 2D/2D layered P-La$_2$Ti$_2$O$_7$ /Bi$_2$WO$_6$ contact heterojunctions for upgraded visible-light-driven photocatalysis. *App. Catal. B: Environ.* **2020**, *261*, No. 118244.

(44) Makuła, P.; Pacia, M.; Macyk, W. How To Correctly Determine the Band Gap Energy of Modified Semiconductor Photocatalysts Based on UV−Vis Spectra. *J. Phys. Chem. Lett.* **2018**, *9*, 6814−6817.

(45) Safaralizadeh, E.; Darzi, S. J.; Mahjoub, A. R.; Abazari, R. Visible light-induced degradation of phenolic compounds by Sudan black dye sensitized TiO$_2$ nanoparticles as an advanced photocatalytic material. *Res. Chem. Intermed.* **2017**, *43*, 1197−1209.

(46) Yang, S.; Zhao, H.; Dong, F.; Tang, Z.; Zha, F. Three-dimensional flower-like OMS-2 supported Ru catalysts for application

in the combustion reaction of o-dichlorobenzene. *Catal. Sci. Technol.* **2019**, *9*, 6503−6516.

(47) Chang, L.; Pu, Y.; Shen, G.; Cui, Y.; Xu, S. Excellent Adsorption-Photocatalysis Synergistic Activity of 3D-3D Flower-like BiOBr/Graphene Hydrogel Composite and the Removal of PBX. *New J. Chem.* **2020**, *44*, 2479 DOI: 10.1039/C9NJ06060J.

(48) Liu, J.; Zhang, S.; Zhao, H.J.A.S.S. Fabricating visible-light photoactive 3D flower-like BiOCl nanostructures via a one-step solution chemistry method at room temperature. *Appl. Surf. Sci.* **2019**, *479*, 247−252.

(49) Zhang, X.; Dou, S.; Li, W.; Wang, L.; Qu, H.; Chen, X.; Zhang, L.; Zhao, Y.; Zhao, J.; Li, Y. Preparation of monolayer hollow spherical tungsten oxide films with enhanced near infrared electrochromic performances. *Electrochim. Acta* **2019**, *297*, 223−229.

(50) Nakakura, S.; Arif, A. F.; Rinaldi, F. G.; Hirano, T.; Tanabe, E.; Balgis, R.; Ogi, T.J.A.P.T. Direct synthesis of highly crystalline single-phase hexagonal tungsten oxide nanorods by spray pyrolysis. *Adv. Powder Technol.* **2019**, *30*, 6−12.

(51) Wang, P.; Cao, Y.; Zhou, X.; Xu, C.; Yan, Q.J.A.S.S. Facile construction of 3D hierarchical flake ball-shaped γ-AgI/Bi$_2$WO$_6$ Z-scheme heterojunction towards enhanced visible-light photocatalytic performance - ScienceDirect. *Appl. Surf. Sci.* **2020**, *531*, 147345.

(52) Han, C.; Ge, L.; Chen, C.; Li, Y.; Xiao, X.; Zhang, Y.; Guo, L.J.A.C.B.E. Novel visible light induced Co$_3$O$_4$-g-C$_3$N$_4$ heterojunction photocatalysts for efficient degradation of methyl orange. *Applied Catalysis B: Environmental* **2014**, *147*, 546−553.

(53) May-Lozano, M.; Lopez-Medina, R.; Mendoza Escamilla, V.; Rivadeneyra-Romero, G.; Alonzo-Garcia, A.; Morales-Mora, M.; González-Díaz, M. O.; Martinez-Degadillo, S. A. Intensification of the Orange II and Black 5 degradation by sonophotocatalysis using Ag-graphene oxide/TiO$_2$ systems. *Chem. Eng. Process. Process Intensif.* **2020**, *158*, No. 108175.

(54) Song, Y.; Qi, J.; Tian, J.; Gao, S.; Cui, F. Construction of Ag/g-C$_3$N$_4$ photocatalysts with visible-light photocatalytic activity for sulfamethoxazole degradation. *Chem. Eng. J.* **2018**, *341*, 547−555.

(55) Cai, A.; Deng, J.; Xu, M.; Zhu, T.; Zhou, S.; Li, J.; Wang, G.; Li, X. Degradation of tetracycline by UV activated monochloramine process: Kinetics, degradation pathway, DBPs formation and toxicity assessment. *Chem. Eng. J.* **2020**, *395*, No. 125090.

(56) Hassan, Z.J.J.o.E.E. Effects of pH on Antibiotic Denitrification and Biodegradation of Sulfamethoxazole Removal from Simulated Municipal Wastewater by a Novel 3D-BER System. *J. Environ. Eng.* **2020**, *146*, No. 04020134, DOI: 10.1061/(ASCE)EE.1943-7870.000182.

(57) Yu, Y.; Wu, K.; Xu, W.; Chen, D.; Fang, J.; Zhu, X.; Sun, J.; Liang, Y.; Hu, X.; Li, R.; Fang, Z. Adsorption-photocatalysis synergistic removal of contaminants under antibiotic and Cr(VI) coexistence environment using non-metal g-C$_3$N$_4$ based nanomaterial obtained by supramolecular self-assembly method. *J. Hazard. Mater.* **2021**, *404*, No. 124171.

(58) Du, C.; Zhang, Z.; Yu, G.; Wu, H.; Chen, H.; Zhou, L.; Zhang, Y.; Su, Y.; Tan, S.; Yang, L.; Song, J.; Wang, S. A review of metal organic framework (MOFs)-based materials for antibiotics removal via adsorption and photocatalysis. *Chemosphere* **2021**, *272*, No. 129501.

(59) Oladipo, A. A.; Ifebajo, A. O. Highly efficient magnetic chicken bone biochar for removal of tetracycline and fluorescent dye from wastewater: Two-stage adsorber analysis. *Journal of Environmental Management* **2018**, *209*, 9−16.

(60) Eniola, J. O.; Kumar, R.; Mohamed, O. A.; Al-Rashdi, A. A.; Barakat, M. A. Synthesis and characterization of CuFe$_2$O$_4$/NiMgAl-LDH composite for the efficient removal of oxytetracycline antibiotic. *Journal of Saudi Chemical Society* **2020**, *24*, 139−150.

(61) Azalok, A. UV-light-induced photocatalytic performance of reusable MnFe-LDO-biochar for tetracycline removal in water. *J. Photochem. Photobiol., A* **2021**, *405*, No. 112976, DOI: 10.1016/j.jphotochem.2020.112976.

(62) Soltani, T.; Tayyebi, A.; Lee, B. K. Photolysis and photocatalysis of tetracycline by sonochemically heterojunctioned BiVO$_4$/

reduced graphene oxide under visible-light irradiation. *J. Environ. Manage.* **2019**, *232*, 713−721.

(63) Yang, Y.; Hu, X.; Zhao, Y.; Cui, L.; Huang, Z.; Long, J.; Xu, J.; Deng, J.; Wu, C.; Liao, W. Decontamination of tetracycline by thiourea-dioxide-reduced magnetic graphene oxide: Effects of pH, ionic strength, and humic acid concentration. *J. Colloid Interface Sci.* **2017**, *495*, 68−77.

(64) Gao, Y. q.; Gao, N. y.; Chu, W. h.; Zhang, Y. f.; Zhang, J.; Yin, D. q. UV-activated persulfate oxidation of sulfamethoxypyridazine: Kinetics, degradation pathways and impact on DBP formation during subsequent chlorination - ScienceDirect. *Chem. Eng. J.* **2019**, *370*, 706−715.

(65) Niu, J.; Li, Y.; Wang, W. Light-source-dependent role of nitrate and humic acid in tetracycline photolysis: Kinetics and mechanism. *Chemosphere* **2013**, *92*, 1423−1429.

(66) Cheng, R.; Kang, M.; Shen, Z.; Shi, L.; Zheng, X. Visible-light-driven photocatalytic inactivation of bacteriophage f2 by Cu-TiO₂nanofibers in the presence of humic acid. *Journal of Environmental Sciences* **2019**, *77*, 383−391.

(67) Motoc, S.; Ianasi, C.; Baciu, A.; Delcioiu, C.; Sacarescu, L.; Putz, A. M.; Manea, F. HUMIC ACID REMOVAL FROM WATER BY SORPTION AND PHOTOCATALYSIS UNDER VIS IRRADIATION USING Fe₂O₃/SILICA NANOCOMPOSITE. *Environ. Eng. Manage. J.* **2021**, *20*, 335−345.

(68) Yang, Y.; Zeng, Z.; Zhang, C.; Huang, D.; Zeng, G.; Xiao, R.; Lai, C.; Zhou, C.; Guo, H.; Xue, W.; Cheng, M.; Wang, W.; Wang, J. Construction of iodine vacancy-rich BiOI/Ag@AgI Z-scheme heterojunction photocatalysts for visible-light-driven tetracycline degradation: transformation pathways and mechanism insight. *Chem. Eng. J.* **2018**, *349*, 808−821.

(69) Gao, X.; Guo, Q.; Tang, G.; Peng, W.; Luo, Y.; He, D. Effects of inorganic ions on the photocatalytic degradation of carbamazepine. *J. Water Reuse Desalin.* **2019**, *9*, 301−309.

(70) Deng, Y.; Tang, L.; Zeng, G.; Wang, J.; Zhou, Y.; Wang, J.; Tang, J.; Wang, L.; Feng, C. Facile fabrication of mediator-free Z-scheme photocatalyst of phosphorous-doped ultrathin graphitic carbon nitride nanosheets and bismuth vanadate composites with enhanced tetracycline degradation under visible light. *J. Colloid. Interface Sci.* **2018**, *34*, 219.

(71) Ji, Y.; Yang, Y.; Zhou, L.; Wang, L.; Lu, J.; Ferronato, C.; Chovelon, J. M. Photodegradation of sulfasalazine and its human metabolites in water by UV and UV/peroxydisulfate processes. *Water Res.* **2018**, *133*, 299−309.

(72) DresdenLiu, Y.; He, X.; Duan, X.; Fu, Y.; Fatta-Kassinos, D.; Dionysiou, D.D.J.W.R. Significant role of UV and carbonate radical on the degradation of oxytetracycline in UV-AOPs: Kinetics and mechanism. Kinetics and mechanism. *Water Res.* **2016**, *95*, 195−204, DOI: 10.1016/j.watres.2016.03.011.

(73) Vu, A. T.; Mac, V. H.; Nguyen, T. H.; Nguyen, T. H. Preparation of carnation-like Ag-ZnO composites for enhanced photocatalysis under visible light. *Nanotechnology* **2023**, *34*, 275602.

(74) Prakash, B.; Katoch, V.; Shah, A.; Sharma, M.; Devi, M. M.; Panda, J. J.; Sharma, J.; Ganguli, A. K. Continuous Flow Reactor for The Controlled Synthesis and Inline Photocatalysis of Antibacterial Ag₂S Nanoparticles. *Photochem. Photobiol.* **2020**, *96*, 1273−1282.

(75) Tun, P. P.; Wang, J.; Khaing, T. T.; Wu, X.; Zhang, G. Fabrication of functionalized plasmonic Ag loaded Bi₂O₃/montmorillonite nanocomposites for efficient photocatalytic removal of antibiotics and organic dyes. *J. Alloys Compd.* **2020**, *818*, 152836.

(76) Yentür, G.; Dükkancı, M. Fabrication of magnetically separable plasmonic composite photocatalyst of Ag/AgBr/ZnFe₂O₄ for visible light photocatalytic oxidation of carbamazepine. *Appl. Surf. Sci.* **2020**, *510*, No. 145374.

(77) Rezaei, A.; Rezaei, M. R.; Sayadi, M. H. 3D network structure graphene hydrogel-Fe3O4@SnO₂/Ag via an adsorption/photocatalysis synergy for removal of 2,4 dichlorophenol. *J. Taiwan Inst. Chem. Eng.* **2021**, *121*, 154−167.

(78) Lan, J.; He, B.; Haw, C.; Gao, M.; Khan, I.; Zheng, R.; Guo, S.; Zhao, J.; Wang, Z.; Huang, S.; Li, S.; Kang, J. Band Engineering of ZnO/Si Nanowire Arrays in Z-Scheme Heterojunction for Efficient Dye Photodegradation. *Appl. Surface Sci.* **2020**, *529*, No. 147023.

(79) Xue, Y.; Tang, W.; Gu, H.; Wei, M.; Guo, E.; Lu, Q.; Pang, Y. Flexible Bi₂MoO₆/N-doped carbon nanofiber membrane enables tetracycline photocatalysis for environmentally safe growth of Vigna radiata. *J. Alloys Compd.* **2022**, *902*, No. 163860.

(80) Lu, C. A.; Jw, A.; Xl, A.; Jz, A.; Cz, A.; Xin, H. B.; Hl, C.; Lz, B.; Ying, W. B.; Yha, B. J. G. E. Facile preparation of Ag2S/KTa0.5Nb0.5O3 heterojunction for enhanced performance in catalytic nitrogen fixation via photocatalysis and piezo-photocatalysis - ScienceDirect. *Green Energy Environ.* **2022**, *1630* DOI: 10.1016/j.gee.2022.03.007.

(81) Hao, R.; Wang, G.; Tang, H.; Sun, L.; Xu, C.; Han, D. Template-free preparation of macro/mesoporous g-C₃N₄/TiO₂ heterojunction photocatalysts with enhanced visible light photocatalytic activity. *Appl. Catal. B: Environ.* **2016**, *187*, 47−58.

(82) Natarajan, T. S.; Thampi, K. R.; Tayade, R. J. Visible light driven redox-mediator-free dual semiconductor photocatalytic systems for pollutant degradation and the ambiguity in applying Z-scheme concept. *Appl. Catal. B: Environ.* **2018**, *227*, 296−311.

(83) Natarajan, T. S.; Tayade, R. J. Direct dual CaIn₂S₄/Bi₂WO₆ semiconductor nanocomposites with efficient inter-cross-sectional charge carrier transfer for enhanced visible light photocatalysis. *J. Nanopart. Res.* **2021**, *23*, 127 DOI: 10.1007/s11051-021-05252-y.

(84) Zhou, P.; Yu, J.; Jaroniec, M. All-Solid-State Z-Scheme Photocatalytic Systems. *Adv. Mater.* **2014**, 4920−4935.

(85) Guo, H.; Niu, C. G.; Zhang, L.; Wen, X. J.; Liang, C.; Zhang, X. G.; Guan, D. L.; Tang, N.; Zeng, G. M. Construction of direct Z-scheme AgI/Bi₂Sn₂O₇ nanojunction system with enhanced photocatalytic activity: Accelerated interfacial charge transfer induced efficient Cr(VI) reduction, tetracycline degradation and Escherichia coli inactivation. *ACS Sustainable Chem. Eng.* **2018**, *6*, 8003−8018.

(86) Wu, J.; Zhang, H.; Oturan, N.; Wang, Y.; Chen, L.; Oturan, M. A. Application of response surface methodology to the removal of the antibiotic tetracycline by electrochemical process using carbon-felt cathode and DSA (Ti/RuO₂−IrO₂) anode. *Chemosphere* **2012**, *87*, 614−620.

(87) Lu, Z.; Yu, Z.; Dong, J.; Song, M.; Liu, Y.; Liu, X.; Ma, Z.; Su, H.; Yan, Y.; Huo, P. Facile microwave synthesis of a Z-scheme imprinted ZnFe₂O₄/Ag/PEDOT with the specific recognition ability towards improving photocatalytic activity and selectivity for tetracycline. *Chem. Eng. J.* **2018**, *337*, 228−241.

(88) Yang, G.; Liang, Y.; Wang, K.; Yang, J.; Zeng, Z.; Xu, R.; Xie, X. Simultaneous introduction of 0D Bi nanodots and oxygen vacancies onto 1D Bi₆Mo₂O₁₅ sub-microwires for synergistically enhanced photocatalysis. *Chem. Eng. J.* **2021**, *409*, No. 128098.

(89) Zhu, X.-D.; Wang, Y.-J.; Sun, R.-J.; Zhou, D.-M. Photocatalytic degradation of tetracycline in aqueous solution by nanosized TiO₂. *Chemosphere* **2013**, *92*, 925−932.